Materials Today Communications 38 (2024) 108252

Contents lists available at ScienceDirect

Materials Today Communications

journal homepage: www.elsevier.com/locate/mtcomm

Fabrication of enhanced performance Visible-light photodetector based on Ag/ZnS/p-Si/Ag heterojunction grown by chemical bath deposition

Arun Kumar [a], Suhaas Gupta [b], Samrat Mukherjee [c], S. Gaurav [a], S. Shankar [d], Kamal Kumar Kushwah [e], Sujeet Kumar Mahobia [e], Abhineet Samadhiya [f], Stuti Tomar [g], Beer Pal Singh [h], Yogendra K. Gautam [h], Umesh Kumar Dwivedi [i], Sunil Kumar [j], Ravi Kant Choubey [a,*]

[a] *Department of Applied Physics, Amity Institute of Applied Sciences (AIAS), Amity University, Noida Campus, Sector - 125, Noida 201313, Uttar Pradesh, India*
[b] *Department of Condensed Matter Physics, Faculty of Mathematics and Physics, Charles University, Ke Karlovu 5, 12116 Prague, Czech Republic*
[c] *Department of Physics, National Institute of Technology, Patna 800005, Bihar, India*
[d] *Functional Materials Research Laboratory, Department of Physics, ARSD College, University of Delhi-110021, India*
[e] *Department of Applied Physics, Jabalpur Engineering College, Jabalpur 482011, Madhya Pradesh, India*
[f] *Gyan Ganga Institute of Technology and Sciences, Jabalpur, Madhya Pradesh, India*
[g] *Applied Science and Humanities Department, ABES Engineering College, Campus-1, 19th KM Stone, NH-24, Ghaziabad, Uttar Pradesh 201009, India*
[h] *Department of Physics, Chaudhary Charan Singh University, Meerut 250004, India*
[i] *Department of Applied Physics, Amity Institute of Applied Sciences, Amity University, Jaipur, Rajasthan, India*
[j] *Department of Physics, Indira Gandhi University, Meerpur, 122502 Rewari, Haryana, India*

A R T I C L E I N F O

Keywords:
Visible light
Photodetector
ZnS
Heterojunction
Chemical bath deposition

A B S T R A C T

In the present work, ZnS thin films were deposited onto Si-substrate using the chemical bath deposition technique, with a deposition time of 75 min and 100 min, and subsequently the deposited thin films were used to fabricate Ag/ZnS/p-Si/Ag heterojunction devices to study their visible light photodetection properties under illumination intensity of 30 mW/cm^2 and 56 mW/cm^2 under applied forward bias voltage of 0 V and 5 V. Glancing incidence X-ray diffraction analysis confirmed the cubic zinc-blende phase of the deposited thin films, and Scherrer analysis revealed a crystallite size of about 2.4 nm. Surface morphology was studied using scanning electron microscopy and scanning transmission electron microscopy. X-ray photoelectron spectroscopy confirmed the presence of desired Zn^{2+} and S^{2-} chemical species in the deposited thin films. Optical transmittance spectra revealed the higher transmittance of the ZnS thin film deposited for 75 min, while Tauc analysis of the optical absorbance spectra revealed that the deposited thin films had an energy band gap of 3.9 eV. Photoluminescence emission spectra revealed the emission due to recombination transitions via defect-related energy sites. Analysis of the visible light photodetection parameters revealed that the fabricated devices exhibited high performance, especially in terms of response and recovery times, with stable, reproducible and rapid-switching on-off cycles, indicating the potential for application in optical sensing, detection, or communication.

1. Introduction

Out of the various semiconducting materials used in optoelectronic devices and applications, the II-VI compound semiconductor zinc sulfide (ZnS) stands out for being superior in several ways. In the cubic (zinc-blende) phase, it exhibits a direct band gap of ~3.6 eV, which is wider than the direct bandgaps exhibited by most II-VI semiconductor compounds like ZnO (~3.3 eV), CdS (~2.4 eV) and CdTe (~1.5 eV), and commonly used III-V semiconductor compounds like InP (~1.3 eV) and GaAs (~1.4 eV). This spectacularly wide band gap can be made wider due to quantum confinement effects when the ZnS material is restricted to the nano-size regime, as in the case of thin films. This wide band gap leads to the many superior optoelectronic properties of ZnS, like high ultraviolet (UV) absorbance, high refractive index, strong, stable, and

* Corresponding author.
E-mail address: ravikantchoubey@gmail.com (R.K. Choubey).

https://doi.org/10.1016/j.mtcomm.2024.108252
Received 6 December 2023; Received in revised form 23 January 2024; Accepted 27 January 2024
Available online 1 February 2024
2352-4928/© 2024 Elsevier Ltd. All rights reserved.

narrow luminescent emission peaks, fantastic charge carrier mobility, transport, separation, and collection properties, etc., which can also all be tuned and tailored to desired parameters with the help of appropriate doping [1–4]. Other than its superior optoelectronic properties, ZnS is also more environment-friendly and non-cytotoxic in comparison to cadmium-based semiconductor compounds, some of which are commercially used in optoelectronic applications, for example in the buffer layer of CIGS photovoltaic cells. Synthesis techniques for ZnS do not use dangerous or harmful precursors, and the mechanical and chemical stability of ZnS in nano-composite structures like core-shell nanoparticles also makes ZnS an ideal material to be employed in various optoelectronic devices and applications that have an additional requirement of being bio-compatible, for example in optical sensors and detectors employed for labelling, imaging or targeted delivery, photocatalysis, energy storage and conversion [5–9].

Various methods can be used to deposit ZnS thin films, like spin coating, spray pyrolysis, magnetic sputtering, molecular beam epitaxy, chemical vapour deposition, electrochemical deposition, pulsed laser deposition, etc. Every method has its advantages and downsides, and the relevance of the method used depends on the substrate being employed, and the desired physical structure and surface morphology, which in turn has a profound effect on the properties of the deposited ZnS thin film [10–15]. One such synthesis technique is chemical bath deposition, which has certain advantages over the other methods, these being the simplicity of the technique, combined with the relatively low price and time investment required to reliably synthesize high-quality reproducible thin films at ordinary synthesis conditions of relatively low temperatures, ambient atmosphere, and normal air pressure. The authors of the present work, among several other researchers, have previously investigated the effect of changing different synthesis parameters, like synthesis temperature and time, pH level and concentration of the chemical bath, material and inclination of the substrate, etc., to optimize the deposition of ZnS thin films to fabricate high performance heterojunction devices [16–22]. The material and type of substrate employed also play a huge role in the quality of the deposited thin film; in the case of ZnS thin films, Si-substrate is an ideal candidate due to the closely matching lattice constants which promote the formation of a defect-free interface and growth of high-quality crystalline thin film layers.

In nearly all fields of scientific research, light sensors or photodetectors play a vital role in a number of applications, for example in sensing and detection of gases and pollutants, in chemical and biomedical analysis, in optical and thermal imaging, in fiber-optic and laser-based communications, for remote-sensing receivers, in frequency metrology, environmental sensing and astronomy, to name a few; they are also the industry standard for a number of security and control applications. Desirable properties of a high-performance photodetector are high sensitivity and detectivity, rapid response to the presence (and absence) of photons, and reliable, stable and reproducible performance [23–27]. Conventional industry standard semiconductor materials used for photodetection like Ge, GaAs, InGaAs and especially Si are prone to mechanical or performance failure due to being brittle and bulky. They are gradually being phased out by more long-term cost-effective semiconductors like ZnO and CdS that can be used for wider optical ranges and in smaller, more flexible devices. However, these materials still leave something to be desired in terms of responsivity to photons and efficiency of photogeneration and conversion, which once again makes the case for the investigation of the superior semiconducting material ZnS for photodetection applications. Li *et al.* investigated TiO_2 nanotubes (NTs) decorated with an Ag layer using a photochemical method and a ZnS layer using SILAR technique (TiO_2/Ag/ZnS NTs) sandwiched between fluorine-doped TiO_2 (FTO) substrates with a poly sulfide electrolyte solution for application as a fast-response self-powered UV photodetector [28]. Li *et al.* investigated ZnS quantum dots (QDs) synthesized using a wet chemical liquid phase colloidal synthesis method and drop-casted onto a Au/Cr film (with lithographically fabricated interdigital electrodes) deposited onto a quartz substrate for application as a room-temperature UV photodetector [29]. Zhu *et al.* investigated ZnS films prepared using the SILAR method onto $Mg_{0.2}Zn_{0.8}O$ film spin-coated onto quartz substrate with Au interdigital electrodes fabricated using photolithography and frequency magnetron sputtering for application as a high photosensitivity UV photodetector [30]. Jebathew *et al.* investigated pristine and 1% Al, Sn, and Sb doped ZnS thin films synthesized using a nebulizer spray pyrolysis technique with Ag electrodes for application as UV photodetectors [31]. Benyahia *et al.* investigated a ZnO/ZnS microstructure composite deposited onto a glass substrate using a vacuum thermal evaporation technique for application as a self-powered multispectral photodetector [32]. Ismail *et al.* investigated ZnS thin film deposited using pulsed laser deposition onto a multi-walled carbon NT (MWCNT) film drop-cast onto a silicon wafer with Al and In electrodes for application as a multispectral photodetector [33]. Salam and Jayakrishnan investigated ZnS thin films deposited using the SILAR method onto SnO_2:F thin film deposited using spray pyrolysis onto a glass substrate with Ag electrodes for application as a UV and visible light photodetector [34]. The authors of the present work are unaware of any investigation performed on pristine crystalline ZnS thin films deposited using the chemical bath technique onto Si-substrate for application as a visible light photodetector.

To that effect, in the present work, ZnS thin films were deposited onto Si-substrate using chemical bath deposition and were subsequently used to fabricate Ag/ZnS/p-Si/Ag heterojunction device. Photodetection properties of the fabricated heterojunction device were investigated under the visible light illumination, which exhibited the characteristics required of a high performance visible light photodetector.

2. Experimental methods

2.1. Chemical bath deposition of ZnS thin film

Chemical bath deposition method, as described in our previously published reports [21,22,26,27,35], was used to deposit ZnS thin films onto Si-substrate. Ammonium hydroxide (28% NH_3 in H_2O, $\geq$99.99%) supplied by Merck was employed as the complexing agent, while reagent grade zinc acetate dihydrate [$Zn(CH_3CO_2)_2.2\ H_2O$] and thiourea [CH_4N_2S] obtained from Sigma-Aldrich (and used without further purification) were employed as the zinc source and sulfur source, respectively. Briefly, the chemical bath was composed of a solution of zinc acetate (0.1 M) and ammonia, with a dropwise addition of thiourea (0.3 M), and was refluxed at 90 °C for 60 min with constant vigorous stirring. Si-substrates were prepared for deposition with thorough cleaning using ethanol and DI water, 20 min of ultrasonication, and drying in nitrogen atmosphere. ZnS thin films were deposited on the Si-substrate by immersing the substrate in the chemical bath in an inclined manner, at a temperature of 90 °C under constant vigorous stirring. Two ZnS thin film samples were obtained with different deposition times, i.e., one film was allowed to deposit for 75 min, and the other film was allowed to deposit for 100 min. After gently rinsing the thin film samples with DI water to remove lightly adhered particles and impurities, the films were dried in a nitrogen atmosphere and annealed for 30 min at 350 °C.

Specimens for measurements of the STEM were also prepared by the chemical bath deposition method. Carbon copper grids were used for coating of ZnS. The chemical preparation of ZnS was done in the similar way as discussed in the above paragraph and thin ZnS films were prepared. Two different specimens were prepared at two deposition durations of 5 min and 10 min. The thinnest part of the prepared films was used for the measurements of the STEM. However, in the present report, we reported the results obtained at 5 min deposition duration only.

2.2. Fabrication of n-ZnS/p-Si heterojunction device

Silver (Ag) was employed to prepare the ohmic contacts between the deposited film / substrate and the metal electrodes. After annealing of

the films, 7 mm × 8 mm Ag contacts were prepared on opposite sides of heterojunction (on the deposited film and substrate), and subsequently heat treated for 15 min at 300 °C to improve the ohmic contact. Thin copper wires were bonded to the Ag metal contacts with electrically conductive paste to couple the heterojunction device to a Keithley 6517 electrometer. The fabricated devices were illuminated with white light halogen lamp (Havells 150 W) whereas the light intensities were measured with a lux meter.

2.3. Characterizations

Glancing incidence X-ray diffraction (Rigaku Smart Lab GIXRD employing 1.54056 Å Cu-Kα incident radiation, with a scanning rate of 0.02°/s at 40 mA and 40 kV operation) was used to obtain primary phase confirmation of the deposited thin films, and to extrapolate structural parameters of average crystallite size, interplanar spacing, lattice constant, microstrain and dislocation density. Ambios Technology Surface Profiler (Model XP-1 with 1 Å resolution) was employed to measure the thickness of the deposited thin films. Scanning electron microscopy (Zeiss Crossbeam 550 SEM) was employed to observe the surface morphology and to obtain the average grain size of the deposited thin films. Scanning transmission electron microscopy (FEI Titan 80–300 STEM with Cs-correction operating at 200 kV) was employed to further corroborate the phase analysis of the deposited thin film. X-ray photoelectron spectroscopy (Scienta Omicron NanoESCA -II XPS, carried out in a vacuum of 2.4 $\times 10^{-9}$ Torr and referenced against the C1*s* peak at 284.6 eV) was employed to quantitatively identify the oxidation states of the chemical species in the deposited thin film.

Optical transmittance spectra were used to obtain the optical density, while the Tauc plot analysis of the absorption spectra was used to obtain the energy band gap and the absorption edge of the deposited thin films; optical transmittance and absorption spectra were recorded in the range of 290–800 nm using a LabIndia Analytical UV-Vis Spectrophotometer 3092. Photoluminescent emission (PLE) spectra (recorded in the range of 340–550 nm using a PerkinElmer LS-55 with an excitation wavelength of 300 nm) analysis was used to obtain information about the various energy trap states in the forbidden energy band gap of the samples, and the emission colour of the deposited thin films (using a chromaticity diagram). Keithley 6517 electrometer was used to obtain the current-time (I-T) character of the fabricated thin film heterojunction devices to study their photo response of the incident visible light at two different intensities (30 mW/cm^2 and 56 mW/cm^2) under no applied bias and 5 V of applied forward bias conditions.

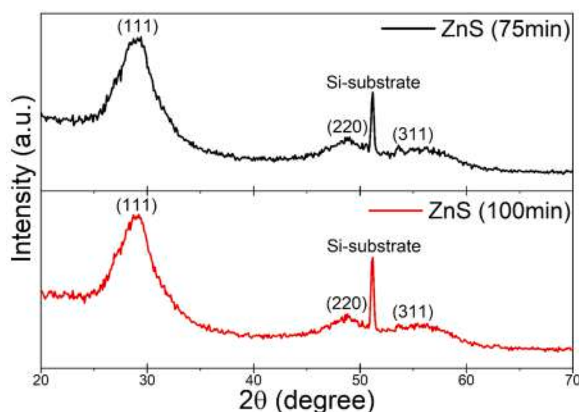

Fig. 1. GIXRD plot of the deposited ZnS thin films on Si-substrate.

3. Results and discussion

3.1. Structure and morphology

Fig. 1 shows the GIXRD plots of the deposited ZnS thin films; singular sharp peak centred at a diffraction angle (2θ) of 51.2° in both the plots corresponds to diffraction from the Si-substrate on which the films were deposited. Three broad peaks can be easily identified in both the plots, centred at 2θ values of about 29.3°, 47.8° and 56.3°, and are attributed to diffraction peaks from the (111), (220) and (311) planes, respectively, of the cubic zinc-blende phase of ZnS. In comparison with the bulk ZnS Powder Diffraction File No. 05–0566, the peak centres show a very slight shift, and a large broadening of peak widths, both of which can arise as a consequence of nano-scale crystallite sizes in the deposited ZnS thin films. The deposited ZnS thin films show a strong preference of growth in the direction of the (111) plane, which can be understood from the high intensity of the characteristic peak. This highest intensity characteristic (111) peak was analyzed to obtain several structural parameters of the deposited ZnS thin films, starting with the lower limit of average crystallite size (D) using the Scherrer formula [36,37], given as

$$D = \frac{k.\lambda}{\beta.\cos\theta} \tag{1}$$

where, β and θ are the full-width at half-maxima (FWHM) and the diffraction angle, respectively, in radians, of the highest intensity characteristic (111) peak, k is the shape factor which we have taken as 0.9 for spherical particles (as confirmed by SEM analysis), and λ is the wavelength of the incident Cu-Kα radiation (= 0.154056 nm). Using the Scherrer formula, we calculated the lower limit of average crystallite size as 2.3 nm and 2.5 nm for the ZnS thin film deposited for 75 min and 100 min, respectively, which is smaller than the Bohr excitonic radius of ZnS (= 2.6 nm), confirming the strong size confinement regime of the deposited ZnS thin films. Further analysis of the highest intensity characteristic (111) peak allowed us to obtain the structural parameters of interplanar spacing (d_{hkl}) and lattice constant (a), given as

$$d_{hkl} = \frac{\lambda}{2\sin\theta} \tag{2}$$

$$a = d_{hkl}\sqrt{h^2 + k^2 + l^2} \tag{3}$$

where, h, k, and l are the Miller indices of the highest intensity characteristic (111) peak; interplanar spacing of 3.0 Å and lattice constant of 5.2 Å was calculated for both the deposited ZnS thin films. In comparison with the bulk ZnS PDF No. 05–0566, the interplanar spacing and lattice constant of both the deposited ZnS thin films exhibit slight contraction, which can again arise as a consequence of the strong size confinement of the ZnS particles to the nano-scale size regime; the ZnS thin film deposited for 100 min exhibits an interplanar spacing and lattice constant which is closer to the values of the same in the bulk ZnS PDF No. 05–0566. Strains and structural impurities in the lattice can also cause shifting of Bragg peak centres, peak width broadening, and contraction in interplanar spacing and lattice constants. The highest intensity characteristic (111) peak was further analyzed to obtain the microstructural parameters of microstrain (ε) and dislocation density (δ), given as

$$\varepsilon = \frac{\beta}{4\tan\theta} \tag{4}$$

$$\delta = \frac{1}{D^2} \tag{5}$$

ZnS thin film deposited for 75 min exhibited a microstrain of 3.0 and a dislocation density of 1.84×10^{17} lines/m^2, while the ZnS thin film deposited for 100 min exhibited a microstrain of 2.9 and a dislocation density of 1.52×10^{17} lines/m^2. The smaller microstructural parameters

of the ZnS thin film deposited for 100 min is to be expected due to the larger size of the crystallites and the smaller contraction in the lattice structure as compared to the ZnS thin film deposited for 75 min

Surface profile analysis of the deposited ZnS thin films revealed that the ZnS thin film deposited for 75 min exhibited a thickness of 425.2 nm, while the ZnS thin film deposited for 100 min exhibited a thickness of 562 nm, which is to be expected due to the increase in deposition time. At higher deposition time the compactness and grain sizes also increase therefore the thickness of the deposited ZnS thin films also increases [21]. The mean deposition rate for both the deposited thin films was approximately 5.6 nm/min. Table 1 summarizes the observed and calculated structural parameters of the deposited ZnS thin films.

Fig. 2 shows the SEM images at different magnifications and the statistical distribution of grain sizes for the deposited ZnS thin films. Primary analysis of the micrographs reveals that the ZnS thin films have been deposited in the form of densely packed spherical grains in the size range of 230–340 nm, consisting of embedded crystallites in the size range of 2–5 nm. Comparison between the micrographs of the ZnS thin film deposited for 75 min (Fig. 2(a-b)) and the ZnS thin film deposited for 100 min (Fig. 2(d-e)) reveals that the increase in deposition time increases the density of the deposited thin film. The ZnS thin film deposited for 100 min completely fills up the few voids visible in the ZnS thin film deposited for 75 min, and subsequent formation of islands of new spherical grains on top of the previous monolayer is observed. Fig. 2(c) and Fig. 2(f) show the statistical distribution of grain sizes and the Gauss fit of the histogram used to obtain the mean size of grains for the deposited ZnS thin films; comparison of the histograms reveals that increasing the deposition time increases both the homogeneity and the mean grain size of the deposited ZnS thin film.

Fig. 3(a-b) shows the STEM images at different magnifications for the prepared ZnS samples, and the corresponding fast Fourier transform (FFT) image and inverse FFT (IFFT) image are shown in Fig. 3(c) and Fig. 3(d), respectively. Even with the poor contrast traditionally exhibited by ZnS, small granular structures in the size range of 2–5 nm can be observed as being embedded throughout the larger grains of the size of a few 100 nanometers. To enhance the clarity of the lattice fringes faintly visible in Fig. 3(b), the power mask method was employed to reduce the noise and separate the spectral frequency of the (111) plane in Fig. 3(c). The lattice fringes of the (111) plane is hence clearly visible with substantial noise reduction in Fig. 3(d) and exhibit an interplanar spacing of 0.31 nm.

Table 1
Observed and calculated structural and optical parameters of the deposited ZnS thin films.

PARAMETERS	ZnS (75 min)	ZnS (100 min)
Structural (Scherrer analysis of the highest intensity (111) peak)		
Diffraction angle (2θ)	29.4°	29.2°
Lower limit of average crystallite size (D)	2.33 nm	2.56 nm
Interplanar spacing (d_{111})	3.03 Å	3.05 Å
Lattice constant (a)	5.24 Å	5.28 Å
Microstrain (ε)	3.04	2.97
Dislocation density (δ)	1.84×10^{17} lines/m^2	1.52×10^{17} lines/m^2
Thin film thickness (from surface profiler)	425.21 nm	562.06 nm
Mean grain size (from SEM analysis)	236 nm	332 nm
Optical transmittance and absorbance (Tauc analysis)		
Transmittance at 350 nm	43.66%	27.66%
Transmittance at 700 nm	64.51%	37.48%
Energy band gap (E_g)	3.95 eV	3.91 eV
Absorption edge (λ_a)	313 nm	317 nm
Photoluminescent emission (transition and wavelength, chromaticity)		
Excitonic (CB to VB)	347 nm	347 nm
CB to interstitial sulphur	372 nm	366 nm
Interstitial zinc to VB	407 nm	407 nm
Sulphur vacancy to VB	418 nm	414 nm
CB to zinc vacancy	448 nm	448 nm
Facilitated by dangling bonds	522 nm	521 nm
CIE 1931 colour co-ordinates (x, y)	(0.212, 0.165)	(0.212, 0.166)

3.2. X-ray photoelectron spectroscopy

Fig. 4(a) shows the XPS general survey scan of the ZnS thin film deposited for 75 min and 100 min. High-resolution XPS scan of the ZnS thin film deposited for 75 min are shown in Fig. 4(b-c) for the Zn2p and S2p states, respectively. High-resolution XPS scan of the ZnS thin film deposited for 100 min are shown in Fig. 4(d-e) for the Zn2p and S2p states, respectively. Two peaks can be observed in the high-resolution core spectrum of the Zn2*p* state for both the films, centred at approximately 1022 eV and 1045 eV, attributed to the $Zn2p_{3/2}$ and $Zn2p_{1/2}$ states, respectively. The two doublet binding energies exhibit a spin-orbit splitting energy of 23.12 eV for the ZnS thin film deposited for 75 min and 23.2 eV for the ZnS thin film deposited for 100 min, both of which are extremely close to the standard value for doublet separation in Zn2p states (~22.97 eV) for the bulk cubic zinc-blende ZnS phase [38–40]; these observations confirm the presence of Zn^{2+} ions in the deposited ZnS thin films. While the peaks seem quite symmetric, fitting performed after Tougaard baseline correction shows the existence of a less stable component appearing at a smaller binding energy in both the Zn2p states. From the area under the deconvoluted curves we can determine that the relative percentage of the concentration of the Zn^{2+} ion and the minor component is 82% and 18%, respectively. This component can be attributed to the metallic interstitial impurity atoms of zinc occurring close to the sulphur vacancy sites [41,42], acting as a defect state of paramount importance for luminescent emission and charge transportation properties in the fabricated device. However, the chemical bath deposition method is a wet chemical synthesis route which has been previously reported to produce Zn-O bonds, which could also be the reason behind the smaller concentration component of the Zn2p states [43,44]. The high-resolution core spectrum of the S2p state for both the deposited films can also be deconvoluted into two split spin-orbit peaks while employing a Tougaard baseline correction function to minimize inelastic background, centred at approximately 161.5 eV and 163 eV, attributed to the $S2p_{3/2}$ and $S2p_{1/2}$ states, respectively, corresponding to the Zn-S bond binding energy [40,45].

3.3. UV–visible spectroscopy

Fig. 5(a) shows the optical transmission spectra of the deposited ZnS thin films. ZnS thin film deposited for 75 min exhibits greater transmission (and hence lesser absorption) as compared to the ZnS thin film deposited for 100 min at all wavelengths in the UV and visible optical regions, which is to be expected, considering that the ZnS thin film deposited for 100 min has a greater density of deposited particles than the ZnS film deposited for 75 min, as was observed from the SEM micrographs. Decreasing transparency with increasing deposition time could also be attributed to an increase in scattering losses due to higher surface roughness and crystallinity. In the UV region (<400 nm), the ZnS thin film deposited for 100 min exhibits less than 30% transmittance, while the ZnS thin film deposited for 75 min exhibits more than 40% transmittance. In the visible region (~400–700 nm), the ZnS thin film deposited for 100 min exhibits less than 40% transmittance, while the ZnS thin film deposited for 75 min exhibits greater than 60% transmittance, indicating potential utility for semi-transparent device fabrication in optoelectronic or photovoltaic applications.

Fig. 5(c) and Fig. 5(d) show the Tauc plots of the ZnS thin films deposited for 75 min and 100 min, respectively, used to obtain the energy band gap (E_g) from the UV–visible absorption spectra of the deposited ZnS thin films (Fig. 5(b)) using the Tauc formula [46,47], given as

$$(\alpha h\nu)^n = \beta.(h\nu - E_g) \quad (6)$$

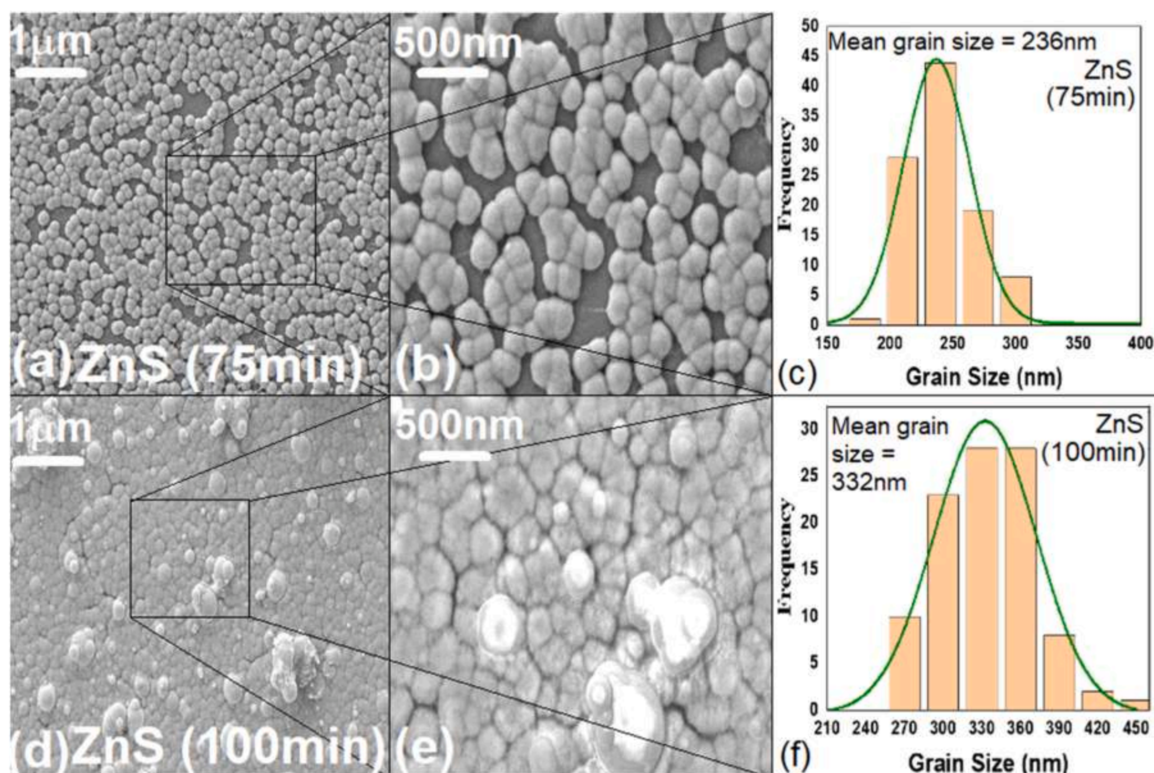

Fig. 2. (a-b) SEM micrographs and (c) histogram of the distribution of grain sizes for the ZnS thin film deposited at 75 min (d-e) SEM micrographs and (f) histogram of the distribution of grain sizes for the ZnS thin film deposited at 100 min.

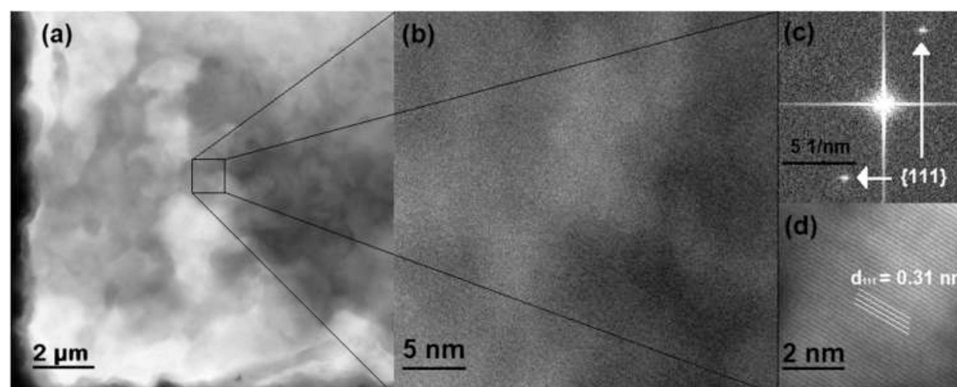

Fig. 3. (a-b) STEM micrograph (c) FFT and (d) IFFT image of the prepared ZnS samples.

where, β is a constant that depends on the probability of transition of an electron upon absorption of a photon having spectral frequency ν, α is the linear absorption coefficient (obtained from the optical absorption spectra), $n = 2$ for direct band gap semiconductors, as is ZnS, and h is the Planck constant; the value of the energy band gap is obtained by plotting a $(\alpha h\nu)^2$ vs. $h\nu$ graph and extrapolating the linear portion of the graph to the x-axis. The obtained energy band gap values of the ZnS thin films deposited for 75 min and 100 min are 3.95 eV and 3.91 eV, respectively; the corresponding absorption edge values ($\lambda_a = hc/E_g$) of the ZnS thin films deposited for 75 min and 100 min are 313 nm and 317 nm, respectively. For the deposited ZnS thin films, the energy band gap values exhibit a considerable increase (and the absorption edge values exhibit a considerable blue shift) with respect to the corresponding value(s) for the bulk cubic zinc-blende phase of ZnS (~3.6 eV and ~344 nm). This increase in energy band gap is in accordance with the strong quantum-confinement theory, which is a manifestation of the strong size-confinement of the crystallites of the deposited ZnS thin films to the nano-size regime, as observed in the structural characterizations. Table 1 summarizes the observed and calculated optical transmittance and absorption parameters of the deposited ZnS thin films.

3.4. Photoluminescence spectroscopy

Fig. 6(a) shows the PLE spectra of the deposited ZnS thin films, which is in the form of a continuous spectrum exhibiting several asymmetric emission peaks; the highest intensity peak at about 347 nm is attributed to the emission arising due to the excitonic transition from the conduction band (CB) to the valence band (VB). The luminescent emission of a semiconductor material occurs due to the radiative recombination of electrons and holes. However, due to various shallow mediating defect energy levels in the forbidden energy band gap, electron-hole recombination can take place via different routes, facilitated by non-radiative transition(s) to efficient energy trap sites. Under the effects

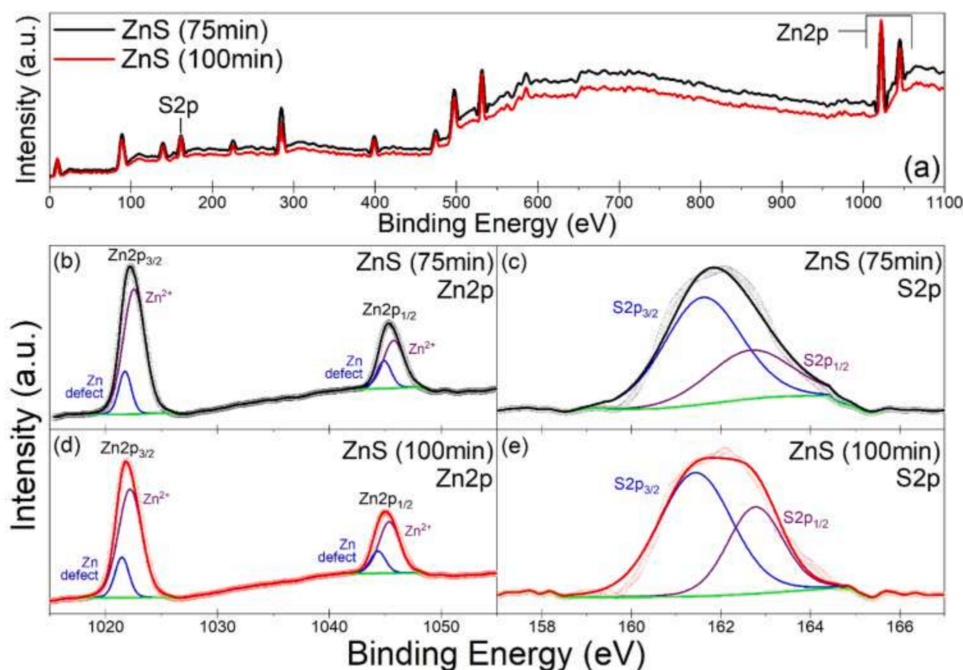

Fig. 4. (a) XPS general survey of the ZnS thin film deposited for 75 min and 100 min (b-c) Deconvoluted high-resolution XPS scan of the ZnS thin film deposited for 75 min of the Zn2*p* and S2*p* states. (d-e) Deconvoluted high-resolution XPS scan of the ZnS thin film deposited for 100 min of the Zn2*p* and S2*p* states.

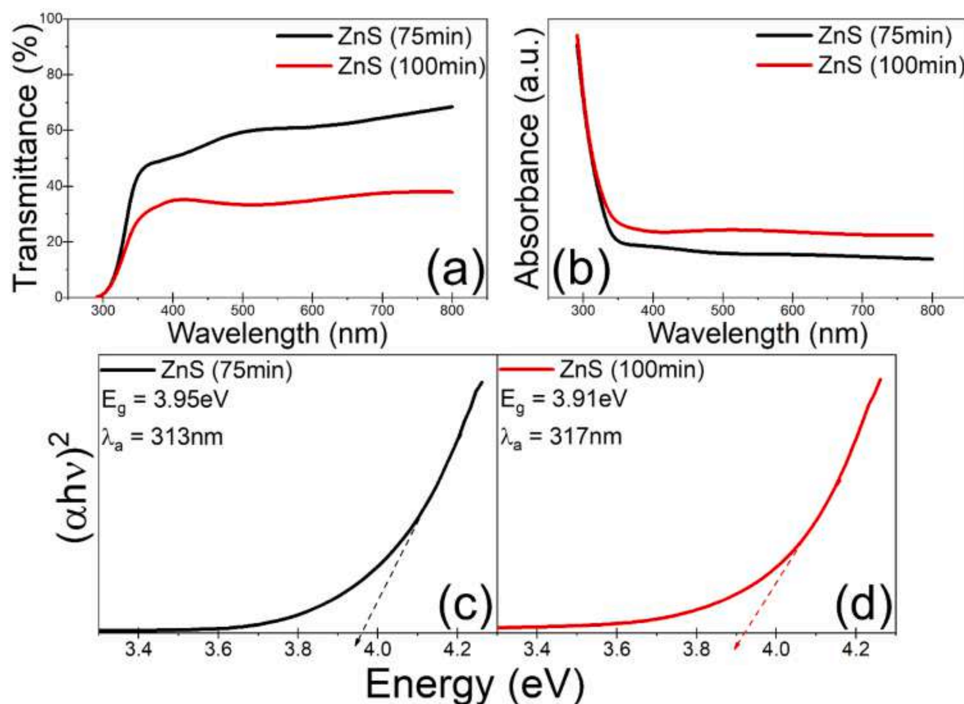

Fig. 5. (a) Optical transmittance, (b) UV-Visible absorbance spectra, and (c-d) Tauc plots of the deposited ZnS thin films at 75 min and 100 min.

of strong-size confinement, as in the case of our deposited ZnS thin films, the increasing surface-to-volume ratio increases the presence of native surface point defects (usually Schottky in nature for ZnS), and hence increases the number of trapping sites facilitating different routes for photo-transitions. The PLE spectra of a nano-sized semiconductor material can thus be deconvoluted using a combination of Gaussian and Lorentzian peaks to represent the various defect-level-mediated radiative recombination mechanisms [8, 48–50].

The minor emission humps at about 369 nm, 416 nm, and 448 nm can be attributed to the transitions facilitated by the surface point defects of interstitial sulfur (I_S), sulfur vacancy (V_S), and zinc vacancy (V_{Zn}), respectively, while the sharp emission peak at about 407 nm can be attributed to the transitions facilitated by the interstitial zinc (I_{Zn}) point defects. Zinc point defects cause less strain (and have larger binding energy) in the native ZnS lattice as compared to sulfur point defects, since zinc ions (Zn^{2+}) have a smaller ionic radius than sulfur ions (S^{2-}). Hence, zinc defect-related energy trap levels occur deeper in the forbidden energy band gap than sulfur interstitial and vacancy-

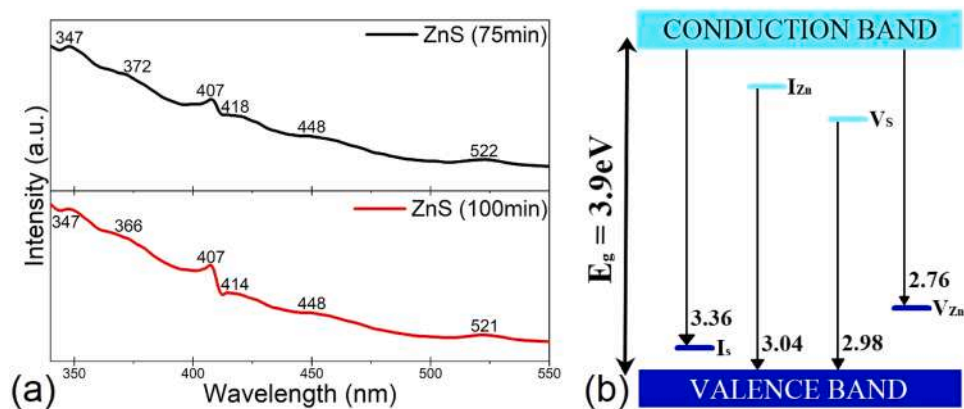

Fig. 6. (a) PLE spectra of the deposited ZnS thin films and (b) schematic illustration of the forbidden energy band gap and defect related shallow energy trapping levels of the deposited ZnS thin films.

related point defect energy trap levels, which appear closer to the VB and CB, respectively. Since the periodic lattice is suddenly terminated at the surface of crystallites and grain boundaries, dangling bond defects are inevitable; however, we can infer a small number of such dangling bond defects in our deposited ZnS thin films from the relatively low intensity of the emission hump at about 521 nm [3,4,6]. Fig. 6(b) shows the energy band diagram of the deposited ZnS thin films with schematically illustrated defect energy levels in the forbidden energy band gap, and Table 1 summarizes the various photoluminescent emission peaks of the deposited ZnS thin films and their attributed transitions.

To obtain information about the potential of the deposited ZnS thin films for LED applications, Commission International del'Eclairage (CIE 1931) chromaticity diagrams were generated from the PLE data, as shown in Fig. 7(a) and Fig. 7(b), for the ZnS thin films deposited for 75 min and 100 min, respectively. The CIE 1931 colour co-ordinates of the ZnS thin films deposited for 75 min and 100 min are (x, y) = (0.212, 0.165) and (x, y) = (0.212, 0.166), respectively, putting them in the blue-violet region, which is most appropriate for application in UV lamps, and can be applied in blue and/or violet colour LEDs.

3.5. Electrical analysis

Fig. 8(a) schematically illustrates the ZnS/p-Si heterojunction device fabricated with Ag metal contacts used to study the visible light photoresponse of the deposited ZnS thin films. We have previously investigated the current-voltage, i.e., I-V response of similarly fabricated Ag/ZnS/p-Si/Ag heterojunction devices and have confirmed the rectifying behavior of the high-performing Schottky diodes hence formed, which operate with a space charge limited current mechanism and exhibit ideality factors close to unity [21,22,26,27,35]. Schottky behavior is ideal for photodetector operation because the Schottky potential barrier at the metal-semiconductor contact efficiently separates electrons and holes to achieve high photocurrents and inhibits electron-hole recombination rate to ensure rapid response times. Fig. 8(b) and Fig. 8(c) show the band diagram of the deposited ZnS thin films in the absence and presence of visible light photons, respectively, illustrating the charge transfer mechanism behind the photoresponse of the ZnS/p-Si heterojunction device. When in the presence of air, the surface of the ZnS thin film adsorbs oxygen molecules which in turn trap free electrons from the thin film surface to make ionized oxygen molecules, leading to the formation of a depletion layer (characterized by an upward bending of band edges and formation of a barrier height with higher potential)

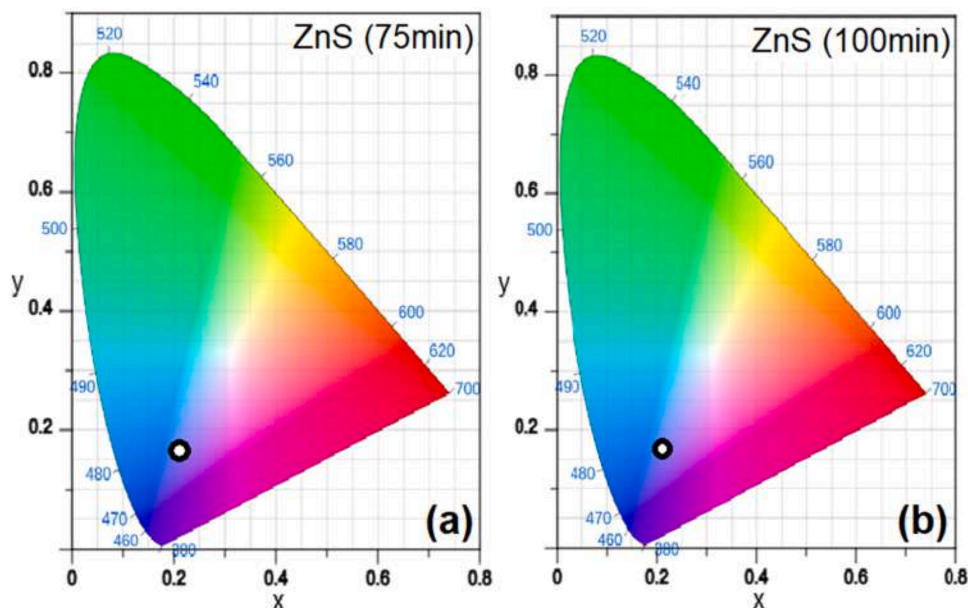

Fig. 7. CIE 1931 chromaticity diagram of the ZnS thin films deposited at (a) 75 min and (b) 100 min.

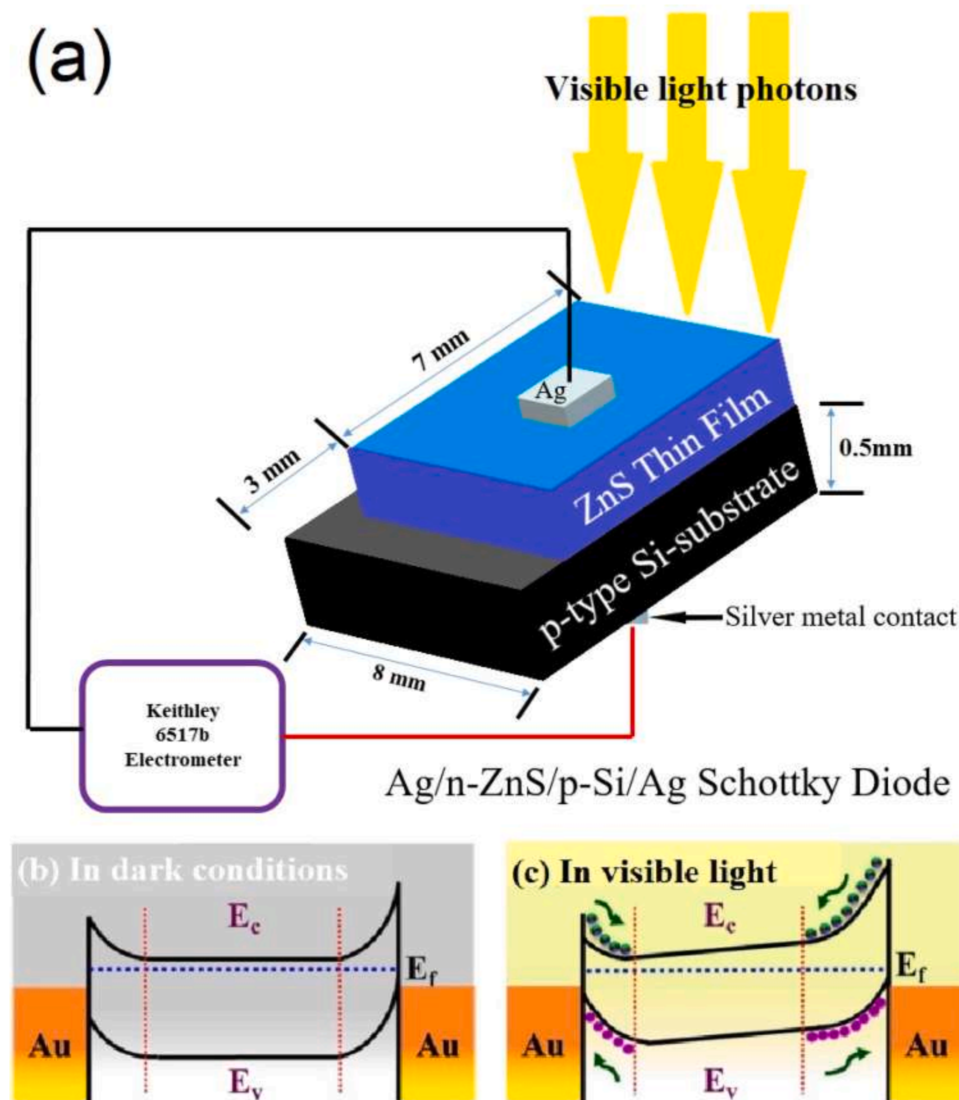

Fig. 8. (a) Schematic illustration of the fabricated Ag/ZnS/p-Si/Ag heterojunction device. Schematic illustration of the bending of energy bands in the deposited ZnS thin film (b) in the absence of visible light photons and (c) when irradiated with visible light photons.

causing low conductivity in the absence of light. When a semiconductor is exposed to photons, they are absorbed by the material to generate electron-hole pairs, which are subsequently separated by the intrinsic or externally applied electric field to produce a current in the device proportional to the incident light intensity. Oxygen desorption is caused by free holes migrating to the surface, leading to increased photocurrent due to a decrease in the depletion layer width, when electrons are returned to ZnS thin film volume to increase the charge carrier concentration [51,52].

To fully quantify the visible light photoresponse of the deposited ZnS thin films, the current in the device was measured over time, i.e., I-T curves were measured under exposure of 30 mW/cm^2 and 56 mW/cm^2 intensity of visible light, switched on and off in 10 s cycles, under 0 V bias and 5 V forward bias conditions; Fig. 9 shows the I-T curves for the ZnS thin film deposited for 75 min, and Fig. 10 shows the I-T curves for the ZnS thin film deposited for 100 min. The I-T curves for both devices under all conditions show three reliably reproducible on-off cycles over the 60 s, selected from a greater number of similar cycles over a larger time span, for ease of representation and calculation. Preliminary observation reveals that both the devices exhibit strong photoresponse to visible light, as can be clearly seen from the sudden increase in current upon illumination, and the subsequent swift decrease in the same when the light is switched off, at both illumination intensities and voltage biases. Both the devices exhibit rapid and stable response and recovery, made possible by the high-quality fabrication of the thin films and subsequent heterojunction device interface that greatly reduce recombination effects and promote photogeneration and charge carrier collection efficiency. The visible light photodetector performance of the fabricated devices was assessed by calculating certain parameters essential to the figure of merit of photodetectors from the individual I-T curves. These parameters are response current (ΔI), sensitivity (S), response time (τ_r), recovery time (τ_d), responsivity (R), specific detectivity (D^*) and linear dynamic range (LDR), given as [53].

$$\Delta I = I_{light} - I_{dark} \tag{7}$$

$$S = I_{light} / I_{dark} \tag{8}$$

$$\tau_r = t_{90\%} - t_{10\%} \tag{9}$$

$$\tau_d = t_{10\%} - t_{90\%} \tag{10}$$

$$R = \frac{\Delta I}{P.A} \tag{11}$$

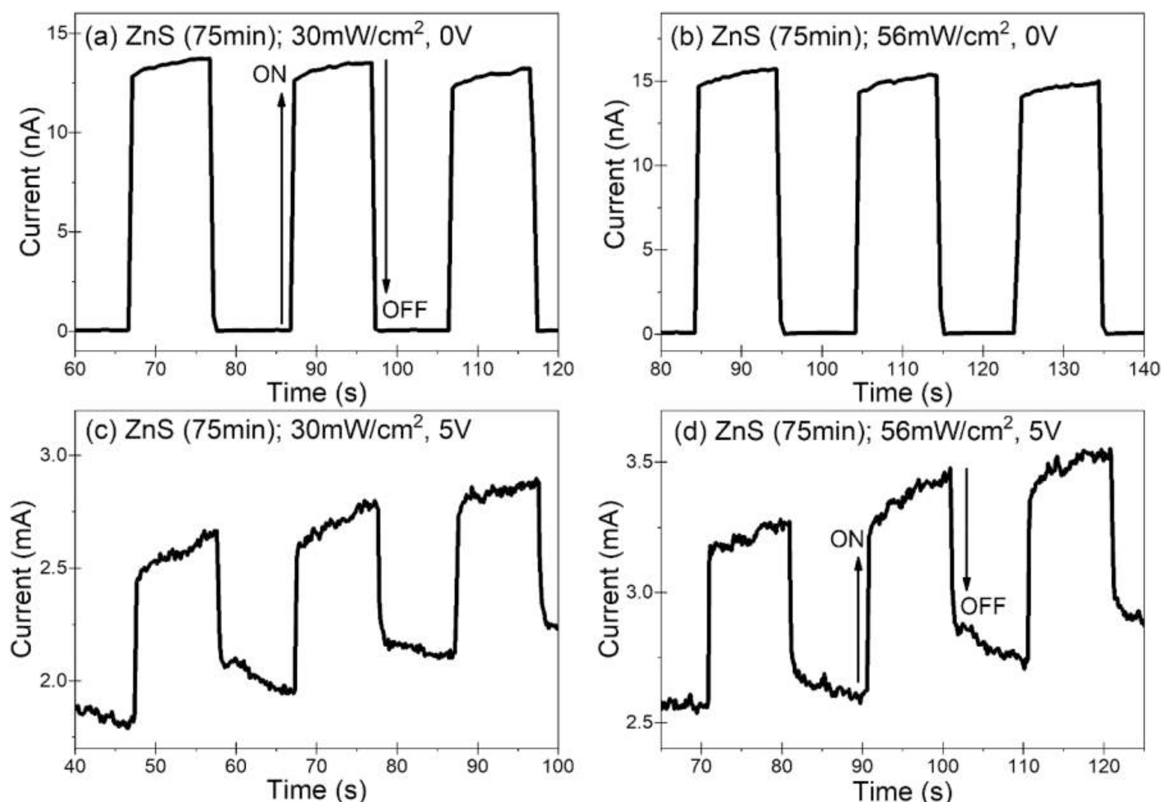

Fig. 9. I-T curve of the heterojunction device fabricated from the ZnS thin film deposited for 75 min under switching illumination of 30 mW/cm^2 and 56 mW/cm^2 visible light at 0 V and 5 V forward bias.

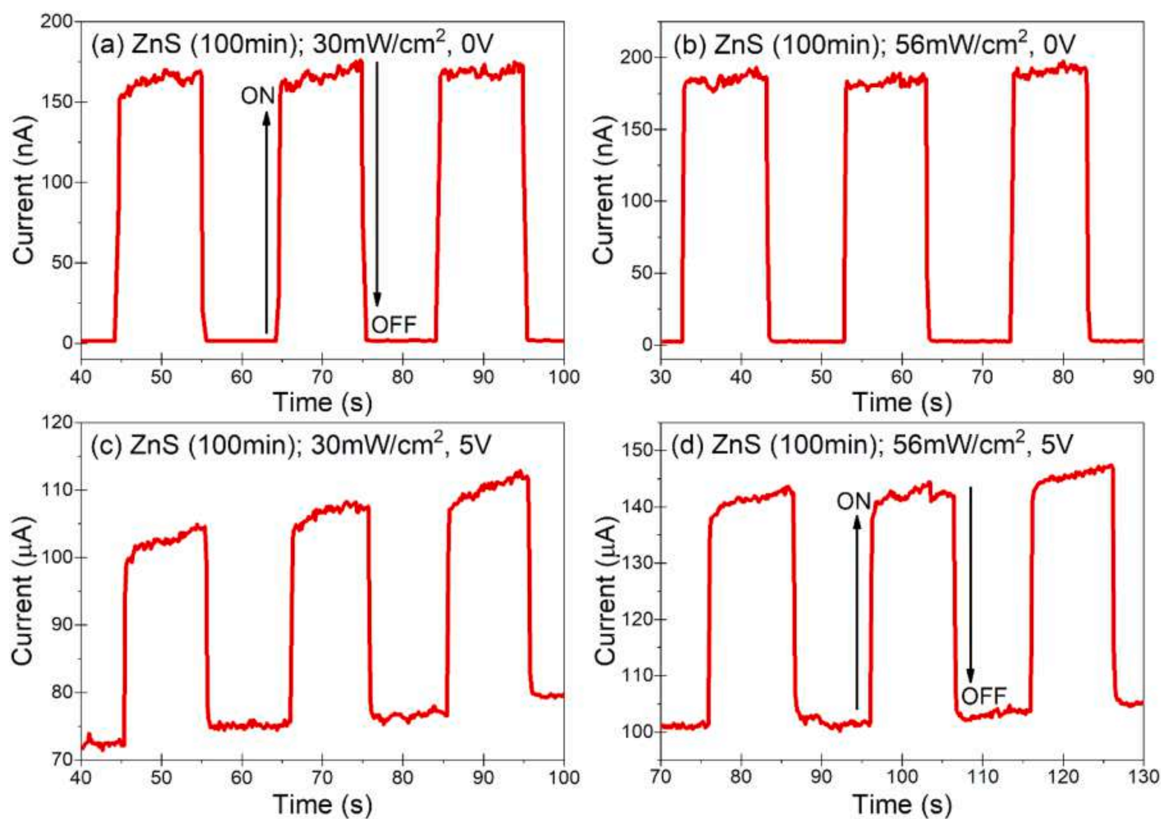

Fig. 10. I-T curve of the heterojunction device fabricated from the ZnS thin film deposited for 100 min under switching illumination of 30 mW/cm^2 and 56 mW/cm^2 visible light at 0 V and 5 V forward bias.

$$D^* = R.\left(\frac{A}{2e.I_{dark}}\right)^{1/2} \quad (12)$$

$$LDR = 20\log S \quad (13)$$

where, I_{light} and I_{dark} are the currents in the device in the presence and absence of visible light illumination, respectively, $t_{90\%}$ and $t_{10\%}$ are the times at 90% and 10% of the I_{light} value, respectively (calculated from the rise and decay of the photocurrent for τ_r and τ_d, respectively), P is the visible light intensity, A is the effective area exposed to the visible light, and e is the elementary charge constant. Table 2 summarizes the calculated photodetection parameters for the fabricated devices, along with the results for equivalent visible light photodetectors from recently published reports to compare with the photodetector performance of our fabricated devices.

The response current of a device is used to distinguish only the photocurrent generated due to visible light illumination, and the sensitivity is used to quantify the signal-to-noise ratio in the presence of photon irradiation; a high-performance photodetector is characterized by having large values for both parameters. In the present work, increasing the intensity of incident visible light markedly increases the response current in both the fabricated heterojunction devices, which is to be expected due to the increase in the number of photogenerated electron-hole pairs and charge carriers. At 0 V bias, the ZnS thin film deposited for 100 min exhibits higher response current than the ZnS thin film deposited for 75 min, clearly indicating the photovoltaic behavior self-powered by the built-in potential of the ZnS/p-Si heterostructure, foregoing any requirement of externally applied voltage for operation as a photodetector. However, at a forward bias voltage of 5 V, the ZnS thin film deposited for 100 min exhibits smaller response current than the ZnS thin film deposited for 75 min, which could arise due to the previously investigated stronger deviation of thicker ZnS thin films from ideal Schottky behavior at higher bias voltages. The ZnS thin film deposited for 100 min also exhibits smaller saturation current at 5 V forward bias voltage as compared to the ZnS thin film deposited for 75 min [21]. In general, the sensitivity decreases with increasing incident light intensity, and with increasing forward bias voltage. This is in accordance with previously published reports on photodetectors [56,57]; Fang *et al.* in fact observed that at a high enough forward bias, the photocurrent and the dark current are indistinguishable, attributed to the injection of a large number of holes that dominate over the photocurrent. At a high value of incident light intensity, the net photocurrent reaches a saturation value, leading to the observed decrease in sensitivity. The ZnS thin film deposited for 100 min still exhibits higher sensitivity than the ZnS thin film deposited for 75 min at 5 V of forward bias voltage, indicating a higher degree of number of photogenerated charge carriers despite lower saturation currents (since the sensitivity is just the ratio of current in the presence of visible light photons to the current in dark conditions).

A rapid photodetection speed, characterised by small response and recovery times, is the parameter most essential to photodetector performance, especially for applications of optical communication, since it describes how quickly the device can detect the presence of photons, and subsequently how quickly the device can return to its original state when the incident light is turned off. Various aspects of the fabricated device, like surface structure, grain size and boundaries, defect trap energy levels and recombination sites in the forbidden energy band gap can affect the response and recovery time of the photodetector [58–60]. In the present work, both the fabricated devices exhibit particularly small response and recovery times, especially when compared to previously reported equivalent visible light photodetectors, indicating the high performance potential of our deposited thin films as rapid-response visible light sensors or optical switches. The general trend of larger recovery times as compared to the response times can be ascribed to the mediation of defect-related trap states which cause a lethargy in the recombination rate of electron-hole pairs. When comparing the response

Table 2
Calculated photoresponse parameters of the prepared ZnS/p-Si heterojunction device.

PHOTO-RESPONSE PARAMETER / SAMPLE CONDITIONS	ZnS (75 min)				ZnS (100 min)				$Zn_{0.95}Mn_{0.05}S$ thin film	ZnO/ ZnS microstructure composite	ZnS TF / SnO_2:F substrate	Bi_2Te_3 nanoplate	MoS_2/ZnO QDs 1 V FB
	0 V bias		5 V forward bias		0 V bias		5 V forward bias		0 V Visible light	0 V Green light	White light 1.1 mW/cm^2	0.5 V FB 650 nm 19.1 mW/cm^2	405 nm 0.075 mW/cm^2
	30 mW/cm^2	56 mW/cm^2	30 mW/cm^2	56 mW/cm^2	30 mW/cm^2	56 mW/cm^2	30 mW/cm^2	56 mW/cm^2	30 mW/cm^2				
Response Current (mA)	12.98×10^{-6}	14.79×10^{-6}	0.64	0.62	165.8×10^{-6}	183.3×10^{-6}	30.18×10^{-3}	39.81×10^{-3}	3.33×10^{-4}	0.2×10^{-3}	14×10^{-3}	0.55×10^{-3}	0.667×10^{-6}
Sensitivity	337.72	301.06	1.31	1.22	101.01	51.85	1.39	1.38	501	66.6	107.22	-	-
Response Time (s)	0.355	0.524	0.246	0.218	0.446	0.269	0.241	0.141	0.76	22.3	0.82	4.1	1.5
Recovery Time (s)	0.501	0.41	0.469	0.474	0.43	0.314	0.246	0.214	0.96	40	0.54	7.4	1.1
Responsivity (mA/W)	7.73×10^{-4}	4.71×10^{-4}	38.25	19.91	9.87×10^{-3}	5.8×10^{-3}	1.79	1.26	7.9×10^{-2}	1.05	7.56	23.43×10^{3}	84
Specific Detectivity (Jones)	5.89×10^{9}	4.01×10^{9}	7.25×10^{10}	1.59×10^{10}	1.02×10^{10}	4.31×10^{9}	8.62×10^{9}	3.07×10^{10}	3.5×10^{9}	2.8×10^{12}	4.75×10^{10}	1.54×10^{10}	1.05×10^{11}
Linear Dynamic Range (dB)	50.57	49.57	2.34	1.72	40.08	34.29	2.86	2.79	54.03	-	-	-	-
Reference	This work								[27]	[32]	[34]	[54]	[55]

and recovery times exhibited by the ZnS thin films deposited for 75 min and 100 min, the slower response and recovery times of the ZnS thin film deposited for 75 min can also be ascribed to the presence of a greater number of structural voids (as observed in the SEM analysis) and defect related energy levels (as observed in the PLE analysis).

The responsivity of a photodetector is described as the response current generated in the device per unit of incident visible light illumination, while the specific detectivity provides information pertaining to the ability of the device to detect feeble signals, affected by the dark current and thermal fluctuation-related noise in the photodetector [61,62]. Sensitivity, which is just the light current to dark current ratio, is not a reliable characteristic to describe the photodetector performance at 0 V bias, since the dark current in such conditions should theoretically be 0 A; in reality, however, the dark current is produced due to the residual charge capacitance in the film and scattering noise due to surface and interface defects. This dark current is too low at lower voltages to distinguish between the noise in the device and background effects. In that regard, the responsivity and specific detectivity are better parameters to judge the figure of merit of photodetector devices [56,57]. In the present work, the sensitivity of the fabricated devices follows the same trend as that of the response current, while the specific detectivity of the ZnS thin film deposited for 100 min is higher than that of the ZnS thin film deposited for 75 min, indicating a better figure of merit and better performance of the device fabricated using the ZnS thin film deposited for 100 min. For all investigated conditions, the specific detectivity is comparable or superior to previously reported equivalent visible light photodetectors. The linear dynamic range of a device describes the scope of signals the device can detect and follows a similar trend to the sensitivity of the fabricated devices. Higher values of the linear dynamic range indicate more efficient light conversion and photogenerated charge carrier separation ability of the device, along with a good signal-to-noise ratio.

4. Conclusions

In conclusion, high-quality ZnS thin films were successfully deposited on Si-substrate with deposition times of 75 min and 100 min. GIXRD analysis confirmed the purity of the cubic zinc-blende phase of the two samples, and Scherrer analysis of the highest intensity (111) diffraction peak revealed a lower limit of average crystallite size of about 2.4 nm. Calculation of lattice parameter and interplanar spacing revealed a slight contraction with respect to values of the same for bulk cubic zinc-blende ZnS values, attributed to the strong size confinement to the nanoscale regime and resulting lattice strain and defects; microstructural properties of microstrain and dislocation density were also obtained. SEM analysis revealed the structural morphology of the deposited thin films to be densely packed spherical grains, with the ZnS thin film deposited for 100 min exhibiting far fewer voids than the ZnS thin film deposited for 75 min. STEM analysis corroborated the phase analysis and interplanar spacing obtained from the GIXRD analysis. XPS spectra confirmed that the chemical species in the deposited thin films were indeed Zn^{2+} and S^{2-}. Optical transmittance revealed the higher absorbance capability of the ZnS thin film deposited for 100 min in the visible spectrum, ascribed to the higher density of grains and thicker film. Tauc analysis of the optical absorbance spectra revealed that the energy band gap of the deposited ZnS thin films was 3.9 eV. PLE spectra of the deposited ZnS thin films revealed a continuous nature beyond the excitonic peak, attributed to the recombination transitions mediated by the defect-related shallow energy trapping sites in the forbidden energy band gap. CIE 1931 chromaticity diagrams revealed that both films mainly emit a blue-violet colour. Ag/ZnS/p-Si/Ag heterojunction devices were fabricated to analyse the visible light photodetection properties of the deposited thin films, studied under two different light intensities (30 mW/cm^2 and 56 mW/cm^2) at two different bias voltages (0 V and 5 V forward bias). Both the devices exhibited stable response currents to the presence of visible light photons, and reproducible fast-switching cycles with spectacularly small rise and decay times when the incident light was turned on and off, respectively, under all conditions. Other photodetection parameters of sensitivity, responsivity, specific detectivity and linear dynamic range were obtained from analysing the I-T curves. All parameters indicated the high photodetector performance of our fabricated device in comparison to other previously reported equivalent visible light photodetectors, which highlights the potential use of ZnS thin films in a number of optical sensing, detection, communication and switching applications.

Author Contributions

All the authors contributed to the present work, conception, and design. Material preparation, data collection and analysis were performed by the authors. The author's contribution is shown below. The first draft of the manuscript was written by Arun Kumar, Suhaas Gupta, Samrat Mukherjee, Ravi Kant Choubey and all other authors helped in the analysis and commented on the previous version of the manuscript. All the authors read and approved the final manuscript. The first draft of the manuscript was written by Arun Kumar, Suhaas Gupta, Samrat Mukherjee, Ravi Kant Choubey and all other authors helped in the analysis and commented on the previous version of the manuscript. All the authors read and approved the final manuscript.

CRediT authorship contribution statement

Kushwah Kamal Kumar: Formal analysis. **Samadhiya Abhineet:** Formal analysis. **Mahobia Sujeet Kumar:** Formal analysis. **Singh Beer Pal:** Formal analysis. **Tomar Stuti:** Data curation. **Dwivedi Umesh Kumar:** Formal analysis. **Kumar Arun:** Writing – original draft, Data curation. **Gautam Yogendra K.:** Formal analysis. **Choubey Ravi Kant:** Writing – review & editing, Supervision, Formal analysis, Data curation. **Mukherjee Samrat:** Writing – review & editing, Supervision, Formal analysis. **Kumar Sunil:** Formal analysis. **Gupta Suhaas:** Writing – original draft. **Shankar S.:** Formal analysis. **Gaurav S.:** Formal analysis.

Declaration of Competing Interest

The authors declare the following financial interests/personal relationships which may be considered as potential competing interests: Ravi Kant Choubey reports financial support was provided by State Council of Science and Technology Uttar Pradesh. Ravi Kant Choubey reports financial support was provided by the Science and Engineering Research Board for funding under Teachers Associateship for Research Excellence (TARE). Ravi Kant Choubey reports financial support was provided by University Grants Commission Department of Atomic Energy Consortium for Scientific Research. Suhaas Gupta reports financial support was provided by Charles University. If there are other authors, they declare that they have no known competing financial interests or personal relationships that could have appeared to influence the work reported in this paper.

Data Availability

Data will be made available on request.

Acknowledgements

The author Ravi Kant Choubey acknowledges the financial support from Council of Science and Technology, Lucknow, Uttar Pradesh, India (Vide No. CST/D-1523), Science and Engineering Research Board for funding under Teachers Associateship for Research Excellence (TARE) File Number: TAR/2023/000265 and UGC-DAE CSR through a Collaborative Research Scheme (CRS) vide project number CRS/2022–23/1105. The author S. Gupta acknowledges the financial support from the Grant Agency of Charles University (GAUK project no. 206423).

References

[1] A. Tiwari, S.J. Dhoble, Critical analysis of phase evolution, morphological control, growth mechanism and photophysical applications of ZnS nanostructures (zero-dimensional to three-dimensional): a review, Cryst. Growth Des. 17 (1) (2017) 381–407.
[2] S.I. Sadovnikov, Synthesis, properties and applications of semiconductor nanostructured zinc sulfide, Russ. Chem. Rev. 88 (6) (2019) 571.
[3] S. Gupta, R.K. Choubey, L.K. Sharma, M.P. Ghosh, M. Kar, S. Mukherjee, Exploring the magnetic ground state of vanadium doped zinc sulphide, Semicond. Sci. Technol. 34 (10) (2019) 105006.
[4] S. Tomar, S. Gupta, S. Mukherjee, A. Singh, S. Kumar, R.K. Choubey, Manganese-doped ZnS QDs: an investigation into the optimal amount of doping, Semiconductors 54 (2020) 1450–1458.
[5] S. Kumar, A. Jain, S. Panwar, I. Sharma, H.C. Jeon, T.W. Kang, R.K. Choubey, Effect of silica on the ZnS nanoparticles for stable and sustainable antibacterial application, Int. J. Appl. Ceram. Technol. 16 (2) (2019) 531–540.
[6] S. Tomar, S. Gupta, S. Mukherjee, A. Singh, S. Kumar, V. Kumar, R.K. Choubey, Optical properties of Silica capped Mn doped ZnS quantum dots, Phys. Scr. 96 (6) (2021) 065802.
[7] S. Kumar, S. Taneja, S. Banyal, M. Singhal, V. Kumar, S. Sahare, S.L. Lee, R. K. Choubey, Bio-synthesised silver nanoparticle-conjugated l-cysteine ceiled Mn: ZnS quantum dots for eco-friendly biosensor and antimicrobial applications, J. Electron. Mater. 50 (2021) 3986–3995.
[8] S. Tomar, S. Gupta, A. Priyam, B. Bhushan, A. Singh, U.K. Dwivedi, R.K. Choubey, Temporal evolution of optical absorption and emission spectra of thiol capped CdTe quantum dots, Appl. Phys. A 128 (10) (2022) 944.
[9] S. Kumar, A. Jain, S. Panwar, I. Sharma, S. Gupta, M. Dopita, R.K. Choubey, Antibacterial studies of ZnO and silica capped manganese doped zinc sulphide nanostructures, Appl. Phys. A 129 (3) (2023) 169.
[10] M.S. Bashar, R. Matin, M. Sultana, A. Siddika, M. Rahaman, M.A. Gafur, F. Ahmed, Effect of rapid thermal annealing on structural and optical properties of ZnS thin films fabricated by RF magnetron sputtering technique, J. Theor. Appl. Phys. 14 (2020) 53–63.
[11] I. Lopez-Quintas, E. Rebollar, D. Ávila-Brande, J.G. Izquierdo, L. Bañares, C. Díaz-Guerra, A. Urbieta, M. Castillejo, R. de Nalda, M. Martín, Femtosecond double-pulse laser ablation and deposition of Co-doped ZnS thin films, Nanomaterials 10 (11) (2020) 2229.
[12] N. Arif, C.S. Fun, Impact on development of ZnS nanoparticles thin film deposited by chemical bath deposition and spin coating, Int. J. Adv. Eng. Nano Technol. 4 (5) (2021) 1–4.
[13] I.D. Simandan, F. Sava, A.T. Buruiana, I. Burducea, N. Becherescu, C. Mihai, A. Velea, A.C. Galca, The effect of the deposition method on the structural and optical properties of ZnS thin films, Coatings 11 (9) (2021) 1064.
[14] A. Najim, B. Hartiti, H. Labrim, S. Fadili, M. Ertuğrul, P. Thevenin, Synthesis of ZnS thin films using the spray pyrolysis technique, J. Mater. Sci.: Mater. Electron. 33 (18) (2022) 15086–15097.
[15] K. Priya, G.K. Rao, G. Sanjeev, The fabrication and characterization of thermal evaporated n-ZnS/p-Si heterojunction and ZnS-Au Schottky photodiodes, Opt. Laser Technol. 157 (2023) 108657.
[16] R.P. Khatri, A.J. Patel, A Comprehensive review on chemical bath deposited ZnS thin film, Int. J. Res. Appl. Sci. Eng. Technol. 6 (3) (2018) 1705–1722.
[17] T. Sinha, D. Lilhare, A. Khare, Effects of various parameters on structural and optical properties of CBD-grown ZnS thin films: a review, J. Electron. Mater. 47 (2018) 1730–1751.
[18] F.G. Hone, T. Abza, "Short review of factors affecting chemical bath deposition method for metal chalcogenide thin films.", Technology 8 (2) (2019) 3.
[19] J. Li, L. Huang, J. Hou, X. Wu, J. Niu, G. Chen, J. Gong, Y. Kong, X. Xiao, Effects of substrate orientation and solution movement in chemical bath deposition on Zn (O, S) buffer layer and Cu (In, Ga) Se2 thin film solar cells, Nano Energy 58 (2019) 427–436.
[20] A. Kumar, D. Pednekar, S. Mukherjee, R.K. Choubey, Effect of deposition time and complexing agents on hierarchical nanoflake-structured CdS thin films, J. Mater. Sci.: Mater. Electron. 31 (2020) 17055–17066.
[21] A. Kumar, S. Mukherjee, S. Sahare, R.K. Choubey, Influence of deposition time on the properties of ZnS/p-Si heterostructures, Mater. Sci. Semicond. Process. 122 (2021) 105471.
[22] A. Kumar, S. Mukherjee, H. Sharma, U.K. Dwivedi, S. Kumar, R.K. Gangwar, R. K. Choubey, Role of deposition parameters on the properties of the fabricated heterojunction ZnS/p-Si Schottky diode, Phys. Scr. 97 (4) (2022) 045819.
[23] T. Dong, J. Simões, Z. Yang, Flexible photodetector based on 2D materials: processing, architectures, and applications, Adv. Mater. Interfaces 7 (4) (2020) 1901657.
[24] B. Ezhilmaran, A. Patra, S. Benny, Sreelakshmi M.R, Akshay V.V, S.V. Bhat, C. S. Rout, Recent developments in the photodetector applications of Schottky diodes based on 2D materials, J. Mater. Chem. C. 9 (19) (2021) 6122–6150.
[25] A. Kumar, M. Kumar, V. Bhatt, D. Kim, S. Mukherjee, J.H. Yun, R.K. Choubey, ZnS microspheres-based photoconductor for UV light-sensing applications, Chem. Phys. Lett. 763 (2021) 138162.
[26] A. Kumar, M. Kumar, V. Bhatt, S. Mukherjee, S. Kumar, H. Sharma, M.K. Yadav, S. Tomar, J.H. Yun, R.K. Choubey, Highly responsive and low-cost ultraviolet sensor based on ZnS/p-Si heterojunction grown by chemical bath deposition, Sens. Actuators A: Phys. 331 (2021) 112988.
[27] A. Kumar, S. Mukherjee, H. Sharma, D.K. Rana, A. Kumar, R. Kumar, R.K. Choubey, Fabrication of low-cost and fast-response visible photodetector based on ZnS: Mn/p-Si heterojunction.", Mater. Sci. Semicond. Process. 155 (2023) 107226.
[28] X. Li, S. Gao, G. Wang, Z. Xu, S. Jiao, D. Wang, Y. Huang, D. Sang, J. Wang, Y. Zhang, A self-powered ultraviolet photodetector based on TiO 2/Ag/ZnS nanotubes with high stability and fast response, J. Mater. Chem. C. 8 (4) (2020) 1353–1358.
[29] R. Li, L. Tang, Q. Zhao, K.S. Teng, S.P. Lau, Facile synthesis of ZnS quantum dots at room temperature for ultra-violet photodetector applications, Chem. Phys. Lett. 742 (2020) 137127.
[30] Y. Zhu, Y. Zhang, L. Yan, D. Zhang, J. Zhou, S. Adimi, S. Ruan, Novel ultraviolet photodetector with ultrahigh photosensitivity employing SILAR-deposited ZnS film on MgZnO, J. Alloy. Compd. 832 (2020) 155022.
[31] A.J. Jebathew, M. Karunakaran, R. Ade, N.D. Jayram, V. Ganesh, Y. Bitla, S. Vinoth, H. Algarni, I.S. Yahia, Optical manipulation of nebulizer spray pyrolysed ZnS thin films for photodetector applications: effect of Al, Sn and Sb doping, Opt. Mater. 117 (2021) 111177.
[32] K. Benyahia, F. Djeffal, H. Ferhati, A. Bendjerad, A. Benhaya, A. Saidi, Self-powered photodetector with improved and broadband multispectral photoresponsivity based on ZnO-ZnS composite, J. Alloy. Compd. 859 (2021) 158242.
[33] R.A. Ismail, A.D. Faisal, S.S. Shaker, Preparation of ZnS-decorated MWCNTs/p-Si hybrid photodetector by pulsed laser deposition, Opt. Mater. 133 (2022) 112998.
[34] J.A. Salam, R. Jayakrishnan, Multispectral self-powered below room-temperature ZnS photodetector, J. Mater. Sci. 58 (12) (2023) 5186–5207.
[35] S. Gupta, A. Kumar, S. Mukherjee, K.K. Kushwah, S.K. Mahobia, P. Patharia, A. Kushwaha, D. Yadav, U.K. Dwivedi, S. Kumar, R.K. Choubey, "Temperature-dependent study of the fabricated ZnS/p-Si heterojunction.", Phys. B: Condens. Matter 657 (2023) 414831.
[36] W.H. Bragg, W.L. Bragg, The reflection of X-rays by crystals, Proc. R. Soc. Lond. Ser. A, Contain. Pap. A Math. Phys. Character 88 (605) (1913) 428–438.
[37] A.L. Patterson, The Scherrer formula for X-ray particle size determination, Phys. Rev. 56 (10) (1939) 978.
[38] S. Ameen, M.S. Akhtar, H.K. Seo, Y.S. Kim, H.S. Shin, Influence of Sn doping on ZnO nanostructures from nanoparticles to spindle shape and their photoelectrochemical properties for dye sensitized solar cells, Chem. Eng. J. 187 (2012) 351–356.
[39] S. Harish, J. Archana, M. Navaneethan, A. Silambarasan, K.D. Nisha, S. Ponnusamy, C. Muthamizhchelvan, H. Ikeda, D.K. Aswal, Y. Hayakawa, Enhanced visible light induced photocatalytic activity on the degradation of organic pollutants by SnO nanoparticle decorated hierarchical ZnO nanostructures, RSC Adv. 6 (92) (2016) 89721–89731.
[40] A.A. Bakly, B.F. Spencer, P. O'brien, The deposition of thin films of cadmium zinc sulfide Cd 1− x Zn x S at 250° C from spin-coated xanthato complexes: a potential route to window layers for photovoltaic cells, J. Mater. Sci. 53 (2018) 4360–4370.
[41] G. Wang, B. Huang, Z. Li, Z. Lou, Z. Wang, Y. Dai, M.H. Whangbo, Synthesis and characterization of ZnS with controlled amount of S vacancies for photocatalytic H2 production under visible light, Sci. Rep. 5 (1) (2015) 8544.
[42] M. Norek, W. Zaleszczyk, G. Łuka, B. Budner, D. Zasada, Tailoring UV emission from a regular array of ZnO nanotubes by the geometrical parameters of the array and Al2O3 coating, Ceram. Int. 43 (7) (2017) 5693–5701.
[43] M. Bär, A. Ennaoui, J. Klaer, T. Kropp, R. Sáez-Araoz, N. Allsop, I. Lauermann, H. W. Schock, M.C. Lux-Steiner, Formation of a ZnS/ Zn (S, O) bilayer buffer on CuInS2 thin film solar cell absorbers by chemical bath deposition, J. Appl. Phys. 99 (12) (2006).
[44] J. Hong, D. Lim, Y.J. Eo, C. Choi, Chemical bath deposited ZnS buffer layer for Cu (In, Ga) Se2 thin film solar cell, Appl. Surf. Sci. 432 (2018) 250–254.
[45] S. Kannan, N.P. Subiramaniyam, M. Sathishkumar, Effect of annealing temperature and Mn doping on the structural and optical properties of ZnS thin films for enhanced photocatalytic degradation under visible light irradiation, Inorg. Chem. Commun. 119 (2020) 108068.
[46] J. Tauc, A. Menth, D.L. Wood, Optical and magnetic investigations of the localized states in semiconducting glasses, Phys. Rev. Lett. 25 (11) (1970) 749.
[47] J. Tauc, A. Menth, States in the gap, J. Non-Cryst. Solids 8 (1972) 569–585.
[48] Z. Wei, Y. Lu, J. Zhao, S. Zhao, R. Wang, N. Fu, X. Li, L. Guan, F. Teng, Synthesis and luminescent modulation of ZnS crystallite by a hydrothermal method, ACS Omega 3 (1) (2018) 137–143.
[49] A.L. Curcio, L.F. da Silva, M.I.B. Bernardi, E. Longo, A. Mesquita, "Nanostructured ZnS: Cu phosphor: correlation between photoluminescence properties and local structure, J. Lumin. 206 (2019) 292–297.
[50] K. Hoang, C. Latouche, S. Jobic, Defect energy levels and persistent luminescence in Cu-doped ZnS, Comput. Mater. Sci. 163 (2019) 63–67.
[51] V. Kumar, I. Rawal, V. Kumar, P.K. Goyal, Efficient UV photodetectors based on Ni-doped ZnS nanoparticles prepared by facial chemical reduction method, Phys. B: Condens. Matter 575 (2019) 411690.
[52] S. Saeed, R. Dai, R.A. Janjua, D. Huang, H. Wang, Z. Wang, Z. Ding, Z. Zhang, Fast-response metal–semiconductor–metal junction ultraviolet photodetector based on ZnS: Mn nanorod networks via a cost-effective method, ACS Omega 6 (48) (2021) 32930–32937.
[53] B.D. Boruah, Zinc oxide ultraviolet photodetectors: rapid progress from conventional to self-powered photodetectors, Nanoscale Adv. 1 (6) (2019) 2059–2085.
[54] J.L. Liu, H. Wang, X. Li, H. Chen, Z.K. Zhang, W.W. Pan, G.Q. Luo, C.L. Yuan, Y. L. Ren, W. Lei, High performance visible photodetectors based on thin two-dimensional Bi2Te3 nanoplates, J. Alloy. Compd. 798 (2019) 656–664.
[55] Y.H. Zhou, Z.B. Zhang, P. Xu, H. Zhang, B. Wang, UV–visible photodetector based on I-type heterostructure of ZnO-QDs/monolayer MoS 2, Nanoscale Res. Lett. 14 (2019) 1–10.

[56] J. Mallows, M. Planells, V. Thakare, R. Bhosale, S. Ogale, N. Robertson, p-Type NiO hybrid visible photodetector, ACS Appl. Mater. Interfaces 7 (50) (2015) 27597–27601.
[57] H. Fang, W. Hu, P. Wang, N. Guo, W. Luo, D. Zheng, F. Gong, M. Luo, H. Tian, X. Zhang, C. Luo, Visible light-assisted high-performance mid-infrared photodetectors based on single InAs nanowire, Nano Lett. 16 (10) (2016) 6416–6424.
[58] Y. Chang, J. Wang, F. Wu, W. Tian, W. Zhai, Structural design and pyroelectric property of SnS/CdS heterojunctions contrived for low-temperature visible photodetectors, Adv. Funct. Mater. 30 (23) (2020) 2001450.
[59] P.P. Biswas, S. Pal, V. Subramanian, P. Murugavel, Polarization driven self-biased and enhanced UV–visible photodetector characteristics of ferroelectric thin film, J. Phys. D: Appl. Phys. 53 (27) (2020) 275302.
[60] H. Ferhati, F. Djeffal, N. Martin, Highly improved responsivity of self-powered UV–Visible photodetector based on TiO2/Ag/TiO2 multilayer deposited by GLAD technique: effects of oriented columns and nano-sculptured surface, Appl. Surf. Sci. 529 (2020) 147069.
[61] D. Kim, K. Park, J.H. Lee, I.S. Kwon, I.H. Kwak, J. Park, Anisotropic 2D SiAs for high-performance UV–visible photodetectors, Small 17 (10) (2021) 2006310.
[62] Z. Li, Y. Zhao, W. Li, Y. Peng, W. Zhao, Z. Wang, L. Shi, W. Fei, A self-powered flexible UV–visible photodetector with high photosensitivity based on BiFeO 3/ XTiO 3 (Sr, Zn, Pb) multilayer films, J. Mater. Chem. A 10 (16) (2022) 8772–8783.